THE JOURNAL OF PHYSICAL CHEMISTRY C
A JOURNAL OF THE AMERICAN CHEMICAL SOCIETY

pubs.acs.org/JPCC
Article

La-Based Perovskite Oxide Catalysts for Alkaline Oxygen Reduction: The Importance of Electrochemical Stability

Jeesoo Seok,[§] Andrés Molina Villarino,[§] Zixiao Shi, Yao Yang, Mahdi Ahmadi, David A. Muller, Francis J. DiSalvo,* and Héctor D. Abruña*

Cite This: https://doi.org/10.1021/acs.jpcc.2c00108

Read Online

ACCESS | Metrics & More | Article Recommendations | Supporting Information

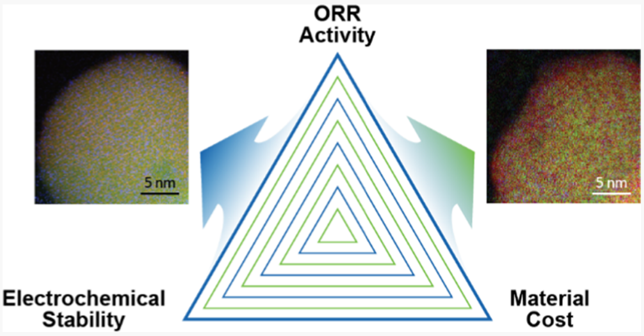

ABSTRACT: Alkaline fuel cells represent a promising energy conversion technology since they enable the use of precious metal-free electrocatalysts for the oxygen reduction reaction. Among these, La-based perovskite oxides, with great compositional and structural tunability, are especially attractive. However, we believe that the current literature lacks a thorough understanding of their inherent (in)stability issues. Here, we report on nine La-based perovskite oxide electrocatalysts for the oxygen reduction reaction, including $LaMO_3$ (M = Mn, Co, Ni) and $LaCo_xM_{1-x}O_3$ (M = Mn, Ni; x = 0.9, 0.5, 0.1). While some exhibited initial promising activity, they all degraded significantly, even after brief electrochemical testing. Through comprehensive structural characterization of $LaCo_{0.9}Mn_{0.1}O_3$, particularly scanning transmission electron microscopy, we found evidence to support a degradation mechanism in which the B-site cation species irreversibly leach from the perovskite under testing conditions. A sample cycled 10 000 times from +0.4 to +1.2 V *vs* reversible hydrogen electrode (RHE) showed an amorphous La oxide shell 1−2 nm thick. Bulk analyses showed that B-site leaching also occurs for samples soaked in 1 M KOH or pure EtOH. The mechanistic insights provided here should help inform the future design of La-based perovskite oxide electrocatalysts for alkaline fuel cells and stress the importance of stability metrics validating claims of promising electrocatalytic activity.

1. INTRODUCTION

Anthropogenic CO_2 has a considerable contribution from the transportation sector.[1] To this end, electric vehicles have been presented as a potential solution.[2] Fuel cells,[3] as a promising alternative to the internal combustion engine (ICE), have much higher energy conversion efficiencies, as well as potentially zero carbon emissions.[4] Specifically, the efficiencies of hydrogen fuel cells (∼60%) are largely dictated by electrochemical reactions and are much higher than those of ICEs (∼20%), which are limited by the Carnot cycle.[5,6] In addition, fast fueling rates (minutes) for hydrogen or other fuels—comparable to an average gasoline car—make them more attractive for transportation applications when compared to batteries, which can require hours to charge.

Prototype fuel cell electric vehicles have so far almost exclusively made use of proton (acidic) exchange membrane (PEM) fuel cells, mainly due to the industrial availability of Nafion.[7] Nevertheless, anion exchange membrane (AEM) fuel cells present multiple benefits that make them promising alternatives to PEM systems.[8] The less corrosive alkaline environments of AEM fuel cells enable the use of non-noble metals as electrocatalysts for the hydrogen oxidation reaction (HOR) and the oxygen reduction reaction (ORR).[9] Additionally, the electroosmotic flow direction in alkaline fuel cells dramatically mitigates the loss in efficiency (∼10%) caused by water crossover,[10,11] which is an intrinsic limitation of acidic fuel cells.[12]

Out of the numerous non-noble metal potential electrocatalysts, the La-based perovskite oxides (general structure $LaMO_3$) appear promising.[13] There have been various reports on the ability of these materials to catalyze reactions such as the oxidation of hydrocarbons,[14] the reduction of nitrogen oxides,[15] and most important to this study, the evolution[16] and reduction[17] of oxygen. The ability to tune their properties, such as electronic and ionic conductivity and catalytic activity, by controlling their elemental composition, makes them especially attractive.[18,19] However, the stability of electrocatalysts in fuel cells is as crucial as their catalytic activity and is a main concern in the fuel cell industry.[20−23] Still, to this day, the long-term stability of these types of materials appears to be

Received: January 6, 2022
Revised: January 20, 2022

very seldom included in studies presenting them as promising catalysts for the ORR.[24]

For perovskite oxides (general structure ABO_3), multiple ORR mechanisms have been proposed. The most common ones revolve around the B-site cation being the active site, with the B-site oxygen vacancy sometimes considered to be the true active site.[17,25] However, the proposed mechanisms generally assume an ideal catalytic cycle, in which the electrocatalytic material is stable throughout testing. In addition, indirect evidence from La-based perovskite oxide single-crystal studies suggests the presence of side reactions that could lead to continuous degradation of the catalyst.[26] In other words, it appears that the stability of the La-based perovskite oxides as ORR electrocatalysts has been generally overlooked in the analyses.

In this study, we have employed initial-*vs*-final-state (*i.e.*, beginning of life, BOL; end-of-life, EOL) evidence to support a reaction mechanism that considers the inherent instability of La-based perovskite oxides under ORR testing conditions in alkaline media. Specifically, we have found evidence for the leaching of the B-site cations under testing conditions, resulting in an amorphous La oxide shell, which, in turn, leads to a continuous decrease in electrocatalytic activity. The information provided here could enable the use of La-based perovskite oxides as practical catalysts for alkaline fuel cells, provided that their instability is mitigated. This work should also underline the paramount significance of studying the long-term stability of seemingly promising catalysts.

2. METHODS

2.1. Materials and Reagents. All chemicals were used as received without any further purification. $La(NO_3)_3{\cdot}6H_2O$ (99.99%), $Co(NO_3)_2{\cdot}6H_2O$ (≥98%), $Mn(NO_3)_2{\cdot}4H_2O$ (≥97.0%), and $Ni(NO_3)_2{\cdot}6H_2O$ (99.999%) were purchased from Sigma-Aldrich. Citric acid (CA; ACS grade), HCl (36.5−38.0 w/w %; ACS plus grade), HNO_3 (68.0−70.0 w/w %; ACS plus grade), acetone (99.5%; ACS grade), and KCl (99.6%; ACS grade) were purchased from Fisher Scientific. KOH (≥85%; ACS grade) was purchased from EMD Millipore. Absolute ethanol (EtOH; 200°; USP grade) was purchased from KOPTEC. Isopropanol (IPA; ACS grade) was purchased from Macron Fine Chemicals. NH_4OH solution (28.0−30.0%; ACS grade) was purchased from EMD Chemicals. Ar (100%; UHP300) and O_2 (100%; UHP300) were purchased from Airgas. Diamond paste (diamond polishing compound; 1 μm), MetaDi Fluid (extender for diamond abrasives), polishing cloth (Microcloth), and sandpaper (CarbiMet 2 240/P280, 400/P800; BuehlerMet II 600/P1200; MicroCut 800/P1500, 1200/P500) were purchased from BUEHLER. Nafion solution (alcohol-based 1100 EW at 5 wt %, with IPA and EtOH) was purchased from the Fuel Cell Store. Deionized (DI) H_2O was obtained from a 7148 Thermo Scientific Barnstead Nanopure dispensing system (18.2 MΩ·cm). Transmission electron microscopy (TEM) grids (LC400-CU-100 Lacey Carbon Film, CU, 400 Mesh, 100 μm) were purchased from Electron Microscopy Sciences. VULCAN XC72R carbon black was purchased from Cabot.

2.2. $LaCoO_3$ Precursor. Briefly, 2.5 mmol (1.08 g) of $La(NO_3)_3{\cdot}6H_2O$, 2.5 mmol (0.73 g) of $Co(NO_3)_2{\cdot}6H_2O$, and 5.0 mmol (0.96 g) of CA were added into a beaker and dissolved in 25 mL of IPA (deep coral clear solution, pH ∼ 1). The solution was stirred and heated to 60 °C using a hot plate until completely dry (light coral solid).

2.3. $LaMnO_3$ Precursor. Briefly, 2.5 mmol (1.08 g) of $La(NO_3)_3{\cdot}6H_2O$, 2.5 mmol (0.63 g) of $Mn(NO_3)_2{\cdot}4H_2O$, and 5.0 mmol (0.96 g) of CA were added into a beaker and dissolved in 25 mL of DI H_2O (clear solution, pH ∼ 1). Then, 3 mL of NH_4OH solution was added at once while stirring. White precipitates formed instantly and then dissolved again (tan solution, pH ∼ 8.5). The solution was heated to ∼130 °C until it became pastelike. The sample was dried in a vacuum oven set to 100 °C (light tan solid).

2.4. $LaNiO_3$ Precursor. Briefly, 2.5 mmol (1.08 g) of $La(NO_3)_3{\cdot}6H_2O$, 2.5 mmol (0.73 g) of $Ni(NO_3)_2{\cdot}6H_2O$, and 5.0 mmol (0.96 g) of CA were mixed in 25 mL of DI H_2O (clear aqua (greenish-blue) solution, pH ∼ 1). Then, a 3 mL aliquot of NH_4OH solution was instantly added. White precipitates formed and most of them dissolved immediately (deep blue solution, pH ∼ 8.5). Then, the solution was heated to ∼130 °C until it became slurry-like (bluish-green slurry). The sample was dried in a vacuum oven set to 100 °C (light tan solid).

2.5. $LaCo_xM_{1-x}O_3$ (M = Mn, Ni; x = 0.9, 0.5, 0.1) Precursors. Briefly, 2.5 mmol (1.08 g) of $La(NO_3)_3{\cdot}6H_2O$, 2.5 mmol of $Co(NO_3)_2{\cdot}6H_2O$ and $Mn(NO_3)_2{\cdot}4H_2O$ or $Ni(NO_3)_2{\cdot}6H_2O$ with a target ratio of 1:9, 5:5, or 9:1, and 5.0 mmol (0.96 g) of CA were added into a beaker and dissolved in 25 mL of DI H_2O. About 3 mL of NH_4OH solution was added to the solution. The solution became cloudy due to precipitates that dissolved again (pH ∼ 8.5). The solution was heated to ∼130 °C until it became very viscous. All samples were dried in a vacuum oven set to 100 °C. The colors of the solutions and solids varied depending on the ratios of precursors.

2.6. La-Based Perovskites. The obtained precursor solids were ground using a mortar and pestle. About a gram of the ground precursor was placed in a clean alumina boat. The boat was placed in the middle of a quartz tube and inside a tube furnace (air). The furnace temperature was ramped up to 600 °C over 60 h, held at 600 °C for 8 h, and then left to cool down to room temperature. After the heat treatment, only ∼30 wt % of the solid was obtained due to the removal of nitrates, hydroxides, and citric acid. All of the final products were black powders, regardless of the elemental composition.

2.7. Catalyst Composites. To finalize the catalyst preparation for electrochemical testing, 40 mg of the perovskite catalyst and 60 mg of carbon black were placed in a zirconium ball mill canister and ball-milled at 400 rpm for 20 min using a Pulverisette 7 classic (Fritsch, Germany). This step was performed for two main reasons: to increase the overall conductivity of the catalyst (now a composite) and to increase the active surface area of the perovskite. The resulting powder was scraped off from the canister with a spatula and placed in a clean vial. All of the final composite products were black powders, regardless of the elemental composition.

2.8. Powder X-ray Diffraction (XRD). The XRD patterns of the synthesized perovskites were obtained using a Rigaku Ultima IV (Rigaku Corporation, Japan) with Cu Kα radiation (40 kV and 44 mA) at a scan rate of 5°/min.

2.9. Low-Magnification TEM. TEM was performed at room temperature using a Tecnai 12 BioTwin transmission electron microscope (Fei Company; Hillsboro, OR), with a LaB_6 electron source at 120 kV, and a Gatan Orius S1000 CCD camera. The electron beam was aligned by hand prior to every set of measurements. Roughly 15 images from different regions within the grids (top, bottom, left, right, center) were analyzed for particle size distribution purposes, and length measurements and counting were performed using ImageJ (https://imagej.nih.gov/ij/download.html). For a typical sample, a spatula tip of the 40 wt % catalyst was transferred to a clean 5 mL vial. An antistatic gun was used when appropriate, to keep the powder from exiting the vial. The vial was then filled to about one-fourth of its volume with EtOH, capped, and sonicated for at least 15 min, while occasionally swirling the vial to ensure homogeneous mixing. About 3 μL of this suspension, typically light gray in color, was then deposited on the grid, held by tweezers that were preemptively rinsed with IPA and dried under an infrared (IR) lamp. The grid was left to dry under the IR lamp and subsequently placed on the appropriate TEM grid box, for analysis.

2.10. High-Angle Annular Dark-Field Scanning Transmission Electron Microscopy and Electron Energy Loss Spectroscopy (HAADF-STEM/EELS). HAADF-STEM/EELS measurements were performed using a Titan microscope (FEI; Hillsboro, ORE) at 300 kV. The HADDF-STEM images were recorded using an FEI Ceta 16M camera. The EELS data were recorded with a GIF Tridiem energy filter (Gatan; Pleasanton, CA) with 0.5 eV/channel energy dispersion. The typical pre-oxygen reduction reaction (ORR) sample was prepared exactly as detailed in Section 2.9. The typical post-ORR sample was prepared in a fashion similar to the one detailed in Section 2.12: The electrode was rinsed with DI H_2O and dried under an IR lamp. Then, a small drop of EtOH was added to the film, and the catalyst was scraped off using a plastic pipette. The appropriate part of this tube was cut and placed inside a clean 5 mL vial, and the vial was filled with EtOH to about one-fourth of its volume. The vial was then sonicated for at least 15 min, with the typical occasional swirling for mixing purposes. About 5−15 μL of this suspension—a very light gray color (almost colorless)—were then deposited on top of the appropriate TEM grid, in increments of 5 μL that were each left to dry under the IR lamp. This grid was then stored for further analysis.

2.11. Image Processing. The STEM images were processed using a Gaussian filter with a radius of 1.5 pixels. The EELS maps were processed in the following steps: first, the original EELS map signals were denoised using Noise2-Void (https://arxiv.org/abs/1811.10980), a self-learned convolutional neural network, with the original data sets used as both the training data and predictions; second, the denoised map signals were background-subtracted using a linear combination of power laws (LCPL) model;[27] and finally, the individual La, Co, and Mn signals were integrated to produce individual maps, which were superimposed to produce composite maps. The EELS depth profiles were plotted with background-subtracted original EELS data using the Cornell Spectrum Imager (CSI),[27] an open-source ImageJ plugin, with 0.7 nm^2 squares average spectra taken at the specified depths. The EELS line profiles were plotted from the EELS maps using a line width of 6 pixels.

2.12. Inductively Coupled Plasma Atomic Emission Spectroscopy (ICP-AES). ICP-AES was performed independently by the Cornell Nutrient Analysis Laboratory (CNAL). For a typical powder sample, 5 mg of the 40 wt % catalyst was placed in a clean 20 mL vial. The aluminum coating under the vial's cap was removed using a spatula. Then, 2 mL of freshly prepared aqua regia (HCl/HNO_3 4:1 v/v) was added to the vial, and the vial was swirled and subsequently left to rest for 30 min, inside a fume hood. After this, 18 mL of DI H_2O was added to the vial, and then the vial was sonicated for 30 min. Since the carbon support does not dissolve in aqua regia, the vial was left to rest at least overnight, and lastly, the top 5 mL of the liquid was transferred to a separate and clean vial using a Pasteur pipette, and this vial was sent for analysis. For the typical electrode sample (after ORR), the rotating disk electrode (RDE) was rinsed with DI H_2O and dried under an IR lamp. Once dry, a small drop of EtOH was added to the film, and the catalyst was scraped off using either a Teflon tube or a plastic pipette. The tip (∼1″) of this tube was then cut and placed inside a 20 mL vial, and the rest of the previous procedure was performed, utilizing 3 mL of fresh aqua regia and 5 mL of DI H_2O, instead of 2 and 18 mL, respectively. For a typical electrolyte sample (after ORR), all of the electrodes were removed from the electrochemical cell, and then 5 mL of fresh aqua regia was added to the cell, evenly split between the three necks. The contents of each neck were thoroughly mixed by dis/charging a Pasteur pipette multiple times, and the walls of each neck were rinsed using this liquid. The whole cell was placed inside a large beaker with sufficient water to match the liquid volume inside the cell, and this large beaker was sonicated for 30 min. After this, the contents of all of the cells' necks were transferred to a 20 mL vial, and the volume of this vial was later reduced to ∼5 mL, using a hotplate to slowly remove the excess solvent (∼2 h). Whenever the final volume of this sample was too low and colorless/light white crystals precipitated (presumably KCl, from the neutralization of HCl and KOH), a minimum amount of DI H_2O was added to the vial, until no solid was present after a few minutes of sonication. The final content of this vial was transferred to a new and clean 20 mL vial and sent to the CNAL for analysis.

2.13. Thermogravimetric Analysis (TGA). TGA for sample $LaCo_{0.9}Ni_{0.1}O_3$ was performed using a Q500 Thermogravimetric Analyzer module (TA Instruments; New Castle, DE), using 100 μL Pt pans and a temperature ramp of 10 °C/min, from room temperature to 700 °C. The analysis was done in an air atmosphere, with a purge flow rate of 60 mL/min. About 100 mg and 1 g of standards were used for weight calibration, and nickel and alumel wires were used for temperature calibration, following the Curie point method. The data were plotted with the temperature axis increasing from right to left, for visual ease.

2.14. X-ray Photoelectron Spectroscopy (XPS). XPS was performed using an ESCA-2SR instrument (Scienta Omicron, Sweden) with an operating pressure of $\sim 1 \times 10^{-9}$ Torr. Monochromatic Al Kα X-rays (1486.6 eV) were generated at 300 W (15 kV; 20 mA). Photoelectrons were collected at a 0° emission angle from a 2 mm analysis spot with a source to an analyzer angle of 54.7°. A hemispherical analyzer determined the electron kinetic energy, using a pass energy of 200 eV for survey scans. All spectra were calibrated with the C_{1s} peak to 284.5 eV and a maximum intensity equal to 1. For the calculation of $O_{sur}/(O_{sur} + O_{latt})$, the peak areas were used. $LaCo_{0.9}Mn_{0.1}O_3$ samples were prepared on a replaceable glassy carbon electrode. Detailed procedures can be found in Sections 2.15−2.21.

2.15. Electrochemical Setup. All of the electrochemical experiments were performed using a custom-made three-neck RDE cell, except for the experiments that involved ICP-AES postanalysis. The latter was performed in a regular (smaller) four-necked cell. A WaveDriver 20 bipotentiostat (Pine Research Instrumentation; Durham, NC) was used, in tandem with an AFMSRCE electrode rotator (Pine Research

Instrumentation; Durham, NC). No IR-drop correction techniques were employed before nor after data acquisition. An AFE3T050GC glassy carbon RDE (Pine Research Instrumentation; Durham, NC) served as the working electrode and was modified accordingly, as described in the next sections. For the experiments that involved XPS postanalysis, an AFE4TQ050 ChangeDisk RDE tip (Pine Research Instrumentation; Durham, NC) was utilized instead, with replaceable SIGRADUR G glassy carbon slugs (HTW Hochtemperatur-Werkstoffe GmbH; Thierhaupten, Germany) that were 5 mm in diameter and about 5 mm in height. These were initially sanded on a mechanical polishing wheel with DI H_2O-wet sandpapers, from coarse to fine, until a mirror finish was attained. A 6" carbon rod (GAMRY Instruments; Warminster, PA), contacted through an alligator clip fixed to the tip using DOUBLE/BUBBLE Extra-Fast Setting Epoxy (Royal Adhesives & Sealants, LLC), served as the counter electrode (CE), and a homebuilt Ag/AgCl (saturated KCl) served as the reference electrode (RE). Nevertheless, all potentials in this manuscript are reported against the reversible hydrogen electrode (RHE). The potential of the Ag/AgCl RE was measured with a source voltmeter against an RREF0021 Ag/AgCl (4 M KCl) "standard" (Pine Research Instrumentation; Durham, NC) before every electrochemical experiment, and ranged from −1.00 to −4.50 mV "*vs* Standard". This standard was just a commercial RE that we currently use exclusively for calibration purposes (Pine reports its potential to be +0.199 V *vs* normal hydrogen electrode (NHE)). The specific readouts of these calibrations were then applied as a correction to the data, along with the equation for the reference potential conversion (which stems from the Nernst equation)

$$E_{\mathrm{RHE}} = E_{\mathrm{Ag/AgCl}} + E^{\mathrm{o}}_{\mathrm{Ag/AgCl}} + 0.059\mathrm{pH} - E_{\mathrm{cal}}$$

where all of the potentials are given in volts, the standard reduction potential for saturated Ag/AgCl is taken to be +0.197 V, and the calibration potential is arbitrarily subtracted, with the calibration electrode always connected to the "COM" terminal of the voltmeter. For any measurement labeled Ar-purged or O_2 saturated, the desired gas was vigorously bubbled close to the bottom of the cell for a minimum of 15 min while rotating the electrode at 1600 rpm, before the start. Throughout such measurements, the solution was continually bubbled but with a lower flow rate and with the gas line closer to the top of the solution (submerged).

2.16. Electrode Modification. All of the glassy carbon electrodes used, including each of the replaceable slugs for the exchangeable RDE rod, were prepared for electrochemical testing following a similar procedure. The electrode was rinsed with small amounts of acetone, EtOH, IPA, and DI H_2O, in the order, and gently blotted/wiped dry with a Kimwipe. Then, the electrode was manually polished using diamond paste and MetaDi fluid on a polishing cloth. After this, the paste was rinsed off with DI H_2O, and the electrode was gently wiped dry with a Kimwipe and further dried under an IR lamp. The lamp was kept at ∼30 cm from the electrode, to avoid excessive heating or uneven drying of any solvent. Once dry, the electrode was mounted on the rotator, placed inside the electrochemical cell with Ar-purged 1 M KOH, and cycled 10 times from +200 to −600 mV *vs* RE at 50 mV/s. The electrode was then removed from the cell, rinsed with DI H_2O, and dried under the IR lamp. Lastly, 5 μL of the appropriate ink (details in the following sections) was very gently drop-cast on the clean glassy carbon surface and allowed to dry under the IR lamp. This cast/dry process was repeated, for a total cast volume of 10 μL, to produce a target catalyst (perovskite) loading of 100 μg/cm^2. Once completed, the electrode was mounted again on the rotator, and submerged in the solution, ready for electrochemical testing.

2.17. Cyclic Voltammetry (CV). Prior to any ORR experiment, the typically modified electrode (see Sections 2.16 and 2.18−2.21), was submerged into the Ar-purged solution and rotated at 1600 rpm for a few minutes. During this time, the Ar gas line was strategically moved around the bottom of the cell, to remove any big bubbles that had formed on the surface of the film upon submersion. After the big bubbles were removed, the gas line was moved closer to the surface of the solution (submerged) and away from the electrode, and the flow rate was reduced. Then, the rotation was stopped, and a 10-cycle CV was performed, at 50 mV/s, from +200 to −600 mV *vs* RE. This corresponds to a window of roughly +1.2 to +0.4 V *vs* RHE.

2.18. ORR. For the typical ORR experiment, an ink of 5 mg/mL (40 wt % catalyst/EtOH) with an added 20 μL of Nafion was used. Once the Ar-purged CV was performed, as described in Section 2.17, the electrode rotator was set to 1600 rpm, the gas line was placed close to the bottom of the cell, and the gas was switched from Ar to O_2. This is critical for producing an O_2-saturated environment since Ar is heavier than O_2 and can easily stay at the bottom of the electrolyte if not properly purged. After a minimum of 15 min of vigorous bubbling, the O_2 gas line was again strategically moved around the bottom of the cell, to remove any big bubbles from the surface of the electrode, and then moved closer to the surface of the solution (submerged) and away from the electrode, with a reduced flow rate. Then, a 10-cycle CV was performed at 5 mV/s and from +200 to −600 mV *vs* RE.

2.19. ORR for ICP-AES. For the typical ORR experiment with ICP-AES postanalysis, an ink of 50 mg/mL (40 wt % catalyst/EtOH) with an added 20 μL of Nafion was used. The typical ink had a total volume of about 100 μL, for the sake of efficient material utilization. For the measurements labeled oxygen-free, the gas was never switched from Ar to O_2, but the procedure was identical to the one detailed in Section 2.18. For the measurements labeled oxygen saturated, the procedure was as described in Section 2.18. For the CVs, 60 cycles were recorded, instead of 10, and the potential windows had different lower potential limits, as stated in the respective plots. The samples were then treated as described in Section 2.12.

2.20. ORR for XPS. For the typical ORR experiment with XPS post-testing analysis, an ink of 5 mg/mL (40 wt % catalyst/EtOH) with an added 20 μL of Nafion was used. The procedure followed was identical to the one detailed in Section 2.18. The only difference was that the ChangeDisk RDE tip was utilized, instead of the regular RDE. To ensure tight fitting of the glassy carbon slug in the RDE tip, the glassy carbon was carefully wrapped with a small amount of Teflon tape prior to its insertion.

2.21. ORR for HAADF-STEM/EELS. For the typical ORR experiment with HAADF-STEM/EELS postanalysis, an ink of 5 mg/mL (40 wt % catalyst/EtOH) with an added 20 μL of Nafion was used. The procedure followed was identical to the one detailed in Section 2.18. The only difference was that 10 000 cycles were performed, at a scan rate of 100 mV/s. Care was taken to maintain a high enough flow of O_2 for analyte saturation purposes but low enough for solution evaporation purposes. The KOH solution was changed periodically.

3. RESULTS AND DISCUSSION

Nine different La-based perovskite oxide nanoparticle catalysts, $LaMO_3$ bimetallics (M = Mn, Co, Ni) and $LaCo_xM_{1-x}O_3$ trimetallics (M = Mn, Ni; x = 0.9, 0.5, 0.1), were synthesized *via* sol−gel chemistry (Figure S1),[28,29] followed by a solid-state reaction at a high temperature. These ratios were selected to produce a library of catalysts with varying B-site compositions, including equimolar and doping-type distributions of the renowned "NMC metals". Briefly, equimolar amounts of A- and total B-site precursors were mixed with excess citric acid (CA) in deionized water. The pH of the solution was adjusted to ∼8.5, and then the solvent was removed through gentle heating and stirring. The resulting solid was then pulverized manually and calcinated at 600 °C in air to produce the perovskite oxides (see the Supporting Information (SI) for details). CA was used as a chelating agent to bind the metal ions and eventually form a homogeneous gel, except for the $LaCoO_3$ sample.[30] Bernard et al. showed that the pH of the precursor solution affects the products after hydrothermal reactions, causing the annealed products to be phase mixed and/or impure.[31] Thus, the pH of the liquid precursor solution was optimized to produce amorphous yet homogeneous solids.[30,31] The B-site cation target composition was controlled by the molar amounts of precursors added to the solution. For example, the $LaCo_{0.5}Mn_{0.5}O_3$ reaction mixture consisted of 2.5 mmol of $La(NO_3)_3$, 1.25 mmol of $Co(NO_3)_2$, and 1.25 mmol of $Mn(NO_3)_2$.

The bulk chemical composition of the samples was experimentally determined *via* inductively coupled plasma atomic emission spectroscopy (ICP-AES) (Table S1), and the perovskite crystal structure was confirmed *via* X-ray diffraction (XRD) (Figure 1). Overall, the chemical composition resulted in ∼1:1 (A/B) ratios for the bimetallic oxides and ∼0.9:0.1/0.5:0.5/0.1:0.9 (B/B′) for the trimetallic oxides. For all of the ICP-AES calculations, the molar amounts of A- and B-site cations were normalized to the amount of La, thus arbitrarily assigning La to be 1.00 mol. It should be noted that a realistic chemical formula for these perovskites would be in the form $AB_xB_y'O_{3-\delta}$, where B and B′ correspond to the different B-site cations, and where δ is proportional to the amount of the so-called oxygen vacancies within the crystal.[32] In the interest of visual simplicity, the remaining text and figures in this manuscript address the different samples using their intended composition formulas (*e.g.*, $LaCo_{0.9}Mn_{0.1}O_3$) and not their real formulas (*e.g.*, $LaCo_{1.01}Mn_{0.11}O_{3-\delta}$). Based on XRD patterns, all of the materials consisted of a single-phase rhombohedral or cubic perovskite structure. Evidence of a cubic cell for samples like $LaNiO_3$ was provided by the apparent merging of the peaks at ∼33°, as described in detail by Zhou and Sunarso.[33] The data are in good agreement with their Goldschmidt tolerance factors (0.841, 0.884, and 0.877 for $LaMnO_3$, $LaCoO_3$, and $LaNiO_3$, respectively, assuming La^{3+}, high-spin Mn^{3+}, and low-spin Ni^{3+} and Co^{3+}, and no other oxidation states).[34,35] According to Hong et al., Mn^{3+} in $LaMnO_3$ is more stable in a high-spin configuration than in a low-spin one, whereas Ni^{3+} and Co^{3+} in $LaNiO_3$ and $LaCoO_3$ prefer a low-spin and an intermediate-spin configuration, respectively.[25] This leads to a much larger perovskite B-site cation radius for Mn^{3+}, compared to Ni^{3+} and Co^{3+} (Table S2).[36] The XRD peaks of $LaNiO_3$ were shifted to lower 2θ angles compared to $LaCoO_3$, which implies that Ni^{3+} had a slightly larger size than Co^{3+}, thus suggesting low spin for Co^{3+} in $LaCoO_3$. The XRD peaks for $LaMnO_3$ appeared at much lower angles, compared to the rest, as the size of Mn^{3+} is significantly larger than those of Ni^{3+} and Co^{3+} (relative lattice expansion). These results correspond well with the reference XRD patterns for bulk rhombohedral La perovskite oxides, as shown in Figure S2, with the notable exception of the cubic samples.

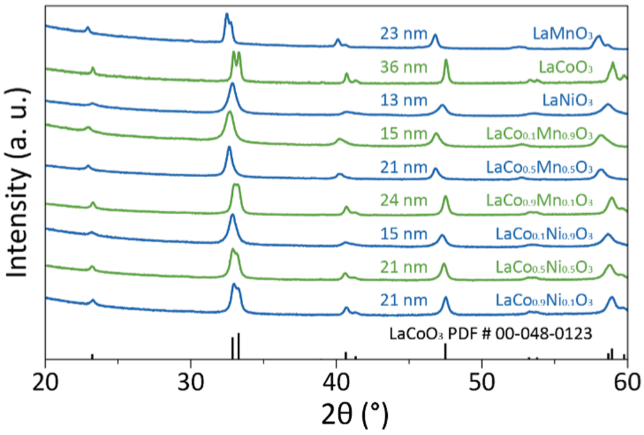

Figure 1. XRD patterns for the perovskite oxides of different (target) compositions synthesized in this study. Grain sizes based on the ∼47° peak.

The peak positions for the trimetallic oxides followed a predictable trend, with a higher Mn^{3+} or Ni^{3+} content resulting in shifts toward lower angles. The (024) peak at around 47° was used to calculate the average grain size of the nanoparticles, using the Scherrer equation. These ranged from 13 to 36 nm, with 21 nm being the average size. $LaCoO_3$ showed a significantly larger grain size than the rest of the samples, and we attribute this to the slightly different synthetic method employed (see the SI for details). Furthermore, the resulting single-phase perovskite oxide powders were mixed with the carbon black support, and ball milled to produce ∼40 wt % catalysts. Thus, all of the data presented in this article correspond to $AB_xB_y'O_{3-\delta}/C$ (40 wt %), unless otherwise stated, with the "/C" also omitted for visual clarity. This loading was confirmed using thermogravimetric analysis (TGA), as shown in Figure S3. The nanoscopic morphology of these catalysts was characterized by transmission electron microscopy (TEM) (Figure S4). A representative image of the $LaCo_{0.9}Ni_{0.1}O_3$ sample shows the catalyst particles embedded on the high surface area Vulcan carbon black, as typical of these composites. The carbon support can be distinguished from the perovskite oxide particles as highlighted in Figure S4. About 15 images across the whole grid area were sampled, and all of the observed particles were counted, for a total of ∼1000 particles, to produce a nanoparticle size distribution (NPSD) chart (Figure S4). The chart for $LaCo_{0.9}Ni_{0.1}O_3$ showed 35 nm as the most prominent particle size (XRD grain size = 21 nm), with the usual thermodynamic tail toward larger sizes, a typical fingerprint for particle growth as studied through LaMer diagrams.[37] This suggests that the "average" particles contain multiple grains.

The alkaline ORR activity for all of the samples was evaluated using rotating disk electrode (RDE) voltammetry (Figure 2), where the cathodic segment corresponding to the

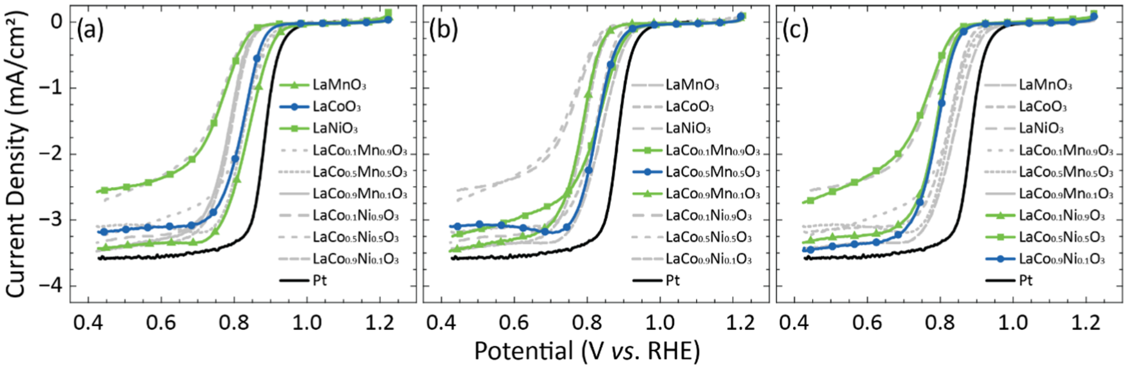

Figure 2. ORR polarization curves of (a) LaMO$_3$ (M = Mn, Co, Ni), (b) LaCo$_x$Mn$_{1-x}$O$_3$ (x = 0.1, 0.5, 0.9), and (c) LaCo$_x$Ni$_{1-x}$O$_3$ (x = 0.1, 0.5 0.9) compared to that of commercial Pt. 0.1 mg$_{\text{oxide}}$/cm^2, 0.025 mg$_{\text{Pt}}$/cm^2, O$_2$-saturated 1 M KOH, 5 mV/s, and 1600 rpm.

second of a total of 10 cycles is shown for each sample. The polarization curve of a commercial 20 wt % Pt/C catalyst (black) is shown, as a standard reference, with a half-wave potential ($E_{1/2}$) of +0.88 V *vs* RHE (reversible hydrogen electrode) measured in 1 M KOH. Figure 2a highlights the three bimetallic oxides. LaNiO$_3$ performed poorly, with the most negative $E_{1/2}$ and onset potential (E_{onset}), evaluated here in a qualitative way as the potential at a current density of -0.25 mA/cm^2. LaMnO$_3$ and LaCoO$_3$ both showed promising electrocatalytic activity, with almost identical $E_{1/2}$'s of about +0.82 V *vs* RHE, just ~60 mV less positive of the Pt reference at the same current density. These $E_{1/2}$ values are also closer to Pt than similar perovskite oxide catalysts in the literature,[17,38,39] indicating superior ORR activity. Furthermore, LaMnO$_3$ showed a slightly more positive E_{onset} (by ~15 mV), relative to LaCoO$_3$, suggesting faster ORR kinetics. Analysis of ORR measurements at varying rotation rates, performed on the LaCoO$_3$ catalyst, yielded a number of electrons transferred (n) of 4.04 ± 0.01 and a kinetic current density (j_k) of 3.81 ± 0.02 mA/cm^2 at +0.8 V *vs* RHE (Figure S5). These values were obtained from the slope and intercept, respectively, of Levich and Koutecký−Levich plots. An n of ~4.0 is indicative of the complete reduction of oxygen to hydroxide. A j_k of ~4 mA/cm^2 at +0.8 V *vs* RHE is comparable to values reported for multiple Pt facets, including (100) and (110),[40] thus suggesting promising electrocatalytic activity.

Figure 2b highlights the trimetallic oxides containing Mn. Analysis of both $E_{1/2}$ and E_{onset} values yielded a catalytic activity order of LaCo$_{0.1}$Mn$_{0.9}$O$_3$ > LaCo$_{0.5}$Mn$_{0.5}$O$_3$ > LaCo$_{0.9}$Mn$_{0.1}$O$_3$, with the performance of the LaCo$_{0.1}$Mn$_{0.9}$O$_3$ catalyst being indistinguishable from that of its bimetallic parent LaMnO$_3$ catalyst. In contrast, the LaCo$_{0.9}$Mn$_{0.1}$O$_3$ catalyst exhibited a decrease of ~40 mV in $E_{1/2}$ and ~30 mV in E_{onset} when compared to its parent LaCoO$_3$ catalyst. Figure 2c highlights the trimetallic oxides containing Ni. For these, the order was LaCo$_{0.9}$Ni$_{0.1}$O$_3$ ≈ LaCo$_{0.1}$Ni$_{0.9}$O$_3$ > LaCo$_{0.5}$Ni$_{0.5}$O$_3$, with the first two catalysts showing virtually identical catalytic activity, both in terms of $E_{1/2}$ and E_{onset}. The observed variations in catalytic activity make us reluctant to make strong claims about a strict activity order as a function of the bulk composition. Ideally, a multivariate analysis that also includes the surface composition and oxygen vacancy content, might be able to better explain these trends. However, such an analysis is beyond the scope of this study. Overall, the Co and Mn bimetallic oxides, as well as the LaCo$_{0.1}$Mn$_{0.9}$O$_3$ trimetallic, were identified as the most promising catalysts from this study, based on initial ORR electrocatalytic activity.

Additional testing of all of the compositions shed light on the importance of electrochemical stability for alkaline ORR catalysis, as shown in Figure 3. After 10 consecutive ORR cycles, a degradation of ~0.30 mA/cm^2 and ~20 mV, in diffusion-limited current density (j_l) and $E_{1/2}$, respectively, was observed for all samples (Table S3). Also, the first cathodic sweep (shown in blue) for numerous compositions was significantly different from the rest of the cycles. We were able to relate these drastic decays in reducing the current density to surface degradation reactions, as discussed below. Overall, the observed decays in terms of j_l and $E_{1/2}$ are substantial and essentially rule out these catalysts as practical candidates for real fuel cell testing, which is inconsistent with previous studies claiming them as being promising alkaline ORR electrocatalysts. Thus, we highlight the importance of a deep understanding of degradation mechanisms for the design of better alkaline ORR electrocatalysts.

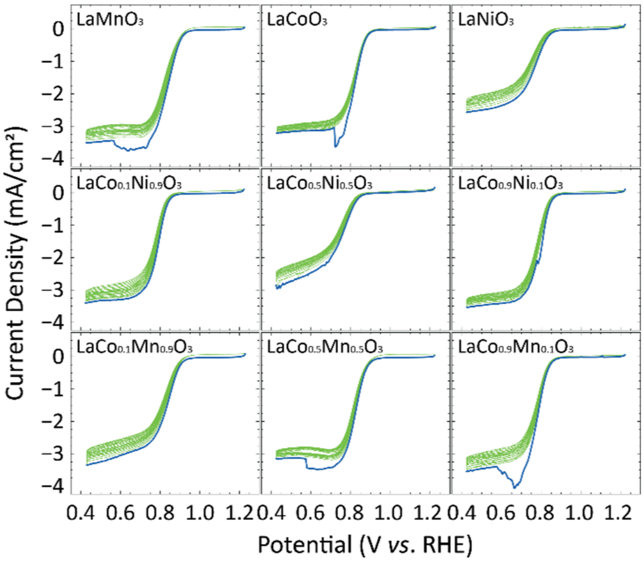

Figure 3. ORR polarization curves of the nine compositions evaluated in this study. Blue denotes the first cathodic segment and green denotes the subsequent consecutive segments. 0.1 mg$_{\text{oxide}}$/cm^2, O$_2$-saturated 1 M KOH, 5 mV/s, 1600 rpm, and 10 cycles.

LaCo$_{0.9}$Mn$_{0.1}$O$_3$ was selected for further testing since it exhibited dramatic changes through the first cycle of the ORR (Figure 3). We employed various characterization techniques before and after electrochemical testing. First, a long-term (10k cycles) durability test was performed by cycling the potential from +1.2 to +0.4 V *vs* RHE at 100 mV/s and 1600 rpm, using a triangular waveform (Figure S6).

The $E_{1/2}$ of the catalyst (measured at −2 mA/cm^2) decreased by ∼75 mV, and the current density decreased by ∼1.25 mA/cm^2. This voltage drop would correspond to a ∼10% decrease in cell voltage (assuming a 0.8 V cell with no loss at the anode), and thus a similar decrease in cell power. While a decrease in ORR current density is harder to quantify in terms of the fuel cell power, a ∼30% drop in the limiting current is very significant. Also, it is worth noting that the double-layer current of the electrode barely changed throughout the test, suggesting little to no change in the catalyst surface area (Figure S6). These results clearly indicate a significant decrease in electrochemical active sites for the ORR under testing conditions, again contrary to what constitutes a promising catalyst.

Second, the metal-based chemical composition of the electrode and the electrolyte samples after testing were analyzed using ICP-AES and compared with the pristine catalyst (Table S4 and Figure S7). All of the "after-testing" samples exhibited elemental compositions indistinguishable from the pristine catalyst, except for the sample that was cycled in an O_2-saturated solution from +1.2 to +0.4 V *vs* RHE, and the sample that was submerged in an Ar-purged solution and not cycled. Both of these samples showed a lower Co/La ratio, indicating significant leaching of Co. Moreover, no La signal was detected for any of the electrolyte samples, while all the electrolyte samples showed Co ions in solution. Similar results have independently been reported by Lopes et al., for perovskite oxides evaluated as oxygen evolution reaction (OER) catalysts.[41] Since the cation solubility of $La(OH)_3$ ($K_{sp} \sim 10^{-19}$; $s \sim 9$ μM) is virtually identical to that of $Co(OH)_2$ ($K_{sp} \sim 10^{-15}$; $s \sim 11$ μM),[42] solubility arguments alone are not sufficient to explain this behavior. On the other hand, half of the electrolyte samples showed Mn ions in solution, whereas the other half did not. Since the ECSA and the amount of electrolyte analyzed for each sample were not exactly known (see the SI for details), and Mn was a dopant in these samples, we cannot exclude the possibility of small amounts of Mn ions—too dilute to be detected *via* ICP-AES—leaching out of all of the samples that showed Co ions in solution. The most surprising finding in this series of experiments was the fact that the leaching of both B-site cations (Co and Mn) was observed even for samples that were not subject to any applied potential, suggesting that the B-site cations of these materials are "soluble" in the tested environments. In other words, these results suggest an inherent instability of these perovskite oxides in alkaline media, as opposed to degradation resulting from the typical particle coalescence, detachment, or Ostwald ripening.[43] Similar leaching of B-site cations was observed for post-ORR $LaMnO_3$ and $LaNiO_3$ samples (Table S5 and Figure S8).

Third, inks made using $LaCo_{0.9}Mn_{0.1}O_3$ were analyzed using X-ray photoelectron spectroscopy (XPS) (Figures 4 and S9−S12). Two distinct features can be observed from the O_{1s} region spectra shown in Figure 4: a decrease in O_{sur}/O_{latt} ratio upon electrochemical testing for the ORR; and a gradual ∼1 eV shift toward lower binding energies for both peaks, in the same order. The O_{sur}/O_{latt} ratio has been utilized previously as a descriptor of perovskite oxide catalytic activity, with the catalyst with the highest ratio performing the best.[44,45] As a general rule, the higher energy O_{1s} peak is assigned to the oxygen surface species physisorbed on B sites, which may form oxygen vacancies during reactions, whereas the lower energy O_{1s} peak is assigned to the lattice oxygen chemically bonded within the crystal.[46−49]

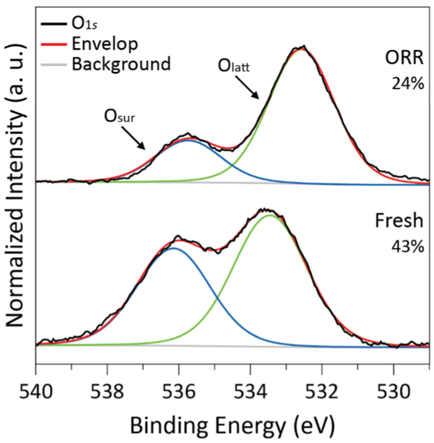

Figure 4. O_{1s} XPS spectra of $LaCo_{0.9}Mn_{0.1}O_3$ inks deposited on glassy carbon. The percentages shown correspond to a ratio of the surface oxygen (blue) and the lattice oxygen (green), following the equation $O_{sur}/(O_{sur} + O_{latt})$. Only the top sample was electrochemically tested. 0.1 mg$_{oxide}$/cm^2, O_2-saturated 1 M KOH, 5 mV/s, 1600 rpm, and 10 cycles from +1.2 to +0.4 V *vs* RHE.

Here, our measurements show a clear decrease in this ratio as a result of testing. Similar degradation was also observed for inks that were tested after being stored in a closed vial for different time periods (Figure S10). Nevertheless, the observed degradation was hindered for the sample that was kept in a freezer at −5 °C, evidencing inherent thermodynamic instability. This would also suggest degradation at an alarming rate in an actual anion exchange membrane fuel (AEMFC) operated at 60−80 °C. The activity trend ($O_{sur}/O_{latt} \propto$ catalytic activity) was further illustrated by the trend of $E_{1/2}$ values of similarly aged samples (Figure S10). Furthermore, the ∼1 eV shift to lower binding energies for both peaks is not surprising, since the chemical environment of the catalyst also changes with testing, as described below. With regard to the relatively high overall position of the O_{1s} peaks, we show that this is a result of the charging behavior of the Nafion binder, as the bare perovskite exhibited the standard ∼529 eV peak for bulk oxygen (Figure S12c).[45,50] We also note that the evaluated O_{1s} peaks are convoluted and include contributions from both the perovskite, the Nafion binder, and the carbon support. Nevertheless, data of an aged sample without perovskite crystals suggest that the support is stable, as opposed to the composite, with the O_{sur}/O_{latt} ratio even increasing slightly with time (Figures S10−S12). Overall, these features point to the thermodynamic instability of oxygen vacancies in these materials under testing conditions, and how this all relates to catalytic activity. These results also emphasize the importance of evaluating catalytic descriptors as a function of time, and not just as predictors of potential catalytic activity.

Fourth and last, $LaCo_{0.9}Mn_{0.1}O_3$ was subject to analysis using high-angle annular dark-field scanning transmission electron microscopy (HAADF-STEM) imaging and electron energy loss spectroscopy (EELS) elemental mapping (Figure 5). While homogeneous distributions of La, Co, and Mn were observed for the pretesting ORR sample, the post-testing ORR sample showed a 1−2 nm thick disordered La oxide shell (Figure 5). A combination of the EELS depth and line profiles,

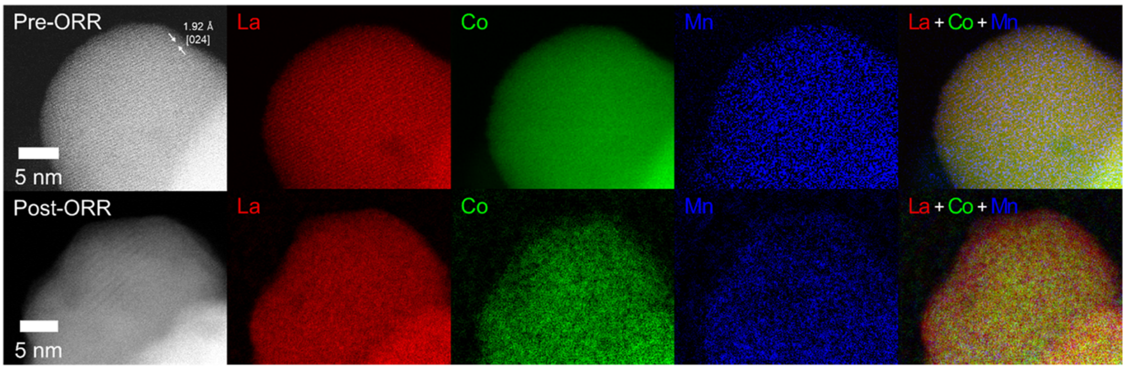

Figure 5. HAADF-STEM images and EELS elemental maps of two different $LaCo_{0.9}Mn_{0.1}O_3$ samples. Only the bottom sample was electrochemically tested. 0.1 mg_{oxide}/cm^2, O_2-saturated 1 M KOH, 100 mV/s, 1600 rpm, and 10k cycles from +1.2 to +0.4 V *vs* RHE.

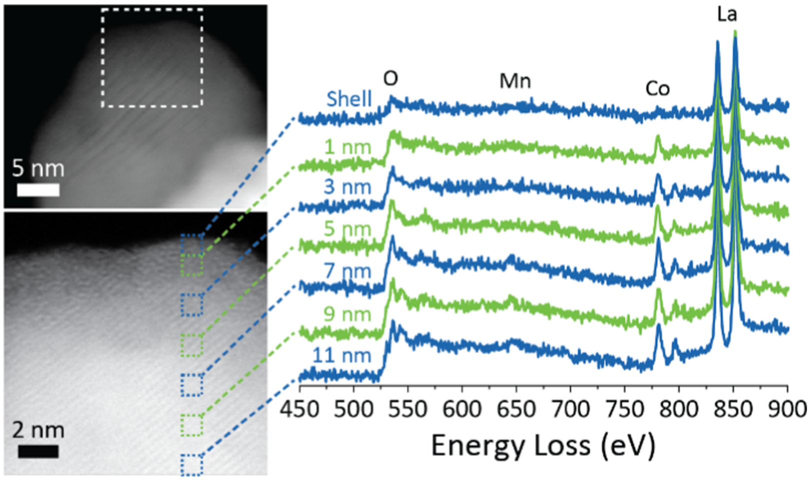

Figure 6. HAADF-STEM image and EELS depth profile of post-ORR $LaCo_{0.9}Mn_{0.1}O_3$. The bottom image corresponds to the region highlighted in the top image. 0.1 mg_{oxide}/cm^2, O_2-saturated 1 M KOH, 100 mV/s, 1600 rpm, and 10k cycles from +1.2 to +0.4 V *vs* RHE.

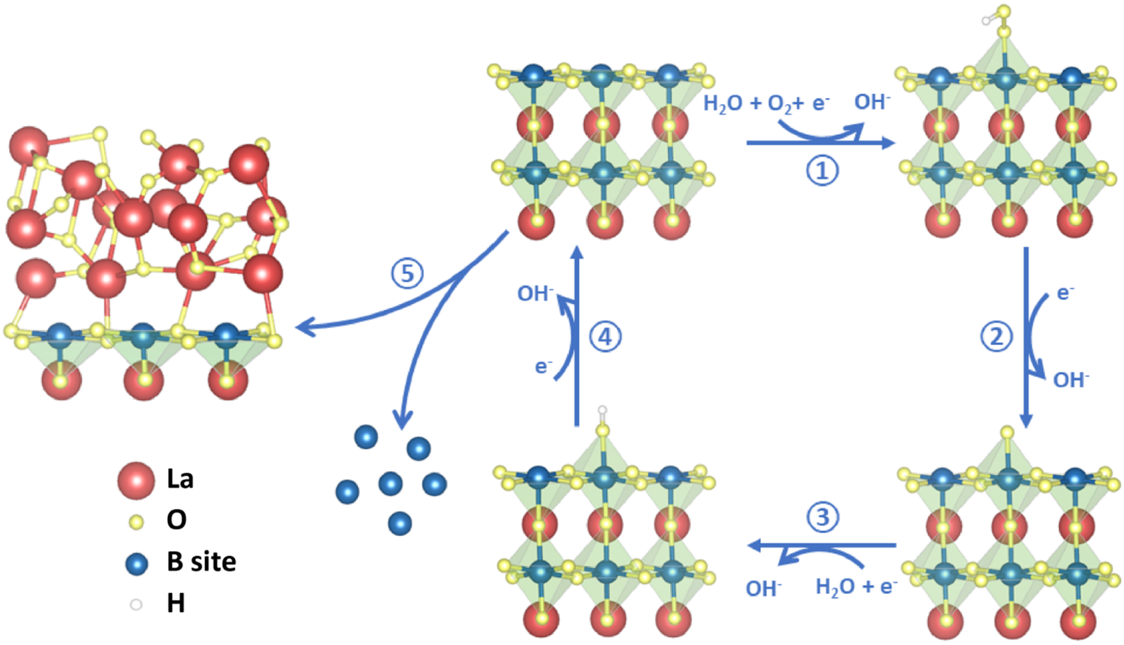

Figure 7. Proposed ORR mechanism for La-based perovskite oxides. Steps 1−4 correspond to the traditional ORR/OER mechanism, where the B-sites catalyze the reactions that lead to the overall conversion of O_2 (step 1) to OH^- (step 4). Step 5 corresponds to the irreversible leaching of B-site cations and subsequent formation of an amorphous La oxide shell, which hinders catalysis.

and high-resolution STEM images of the edges of these particles further served as proof of this (Figures 6, S13, and S14). The lattice fringes observed for the post-testing ORR particle did not extend to the La-rich shell (Figure 6), as opposed to the pretesting ORR particle, which was crystalline throughout (Figure S13). A noticeable feature of the O K-edge EELS peaks for the post-testing ORR sample confirms this, with no peak splitting toward the surface, as opposed to the core, whose O K-edge peak split into three peaks, evidencing the amorphous and crystalline nature on the shell and the core, respectively.[51] This clear lack of peak splitting of the O K-edge signal toward the surface was not observed for the pretesting ORR sample, which also showed a noticeable Co signal at the surface (Figure S13). Furthermore, EELS line profiles for the pretesting and post-testing ORR samples showed different (~2 nm) A- and B-site cation signal onsets after testing but similar onsets before testing, demonstrating the leaching of the B-site cations under testing conditions (Figure S14). Similar leaching of B-site cations has been previously observed for $LaNiO_3$ catalyzing the alkaline OER.[52] According to our results, if the B-site is soluble under alkaline ORR conditions, then it should come as no surprise that it leaches out during some other alkaline reaction, such as the OER. The degradation features discussed here, including surface amorphization and B-site cation leaching, were not observed for the pretesting ORR sample, suggesting its long-term stability (minimum of 1 year) when stored in air, under ambient temperature, pressure, and humidity. These single-particle analyses matched the bulk analyses performed *via* ICP-AES and XPS, which showed irreversible leaching of B-site cations, and a decrease of active sites, respectively. We reiterate the importance of chemical and electrochemical stability as not just a critical factor that should accompany claims of promising catalytic activity but a necessary one.

It is known that surface orientation is important for the catalysis of reactions such as the ORR.[26] Specifically, A-site and B-site terminated surfaces have been a topic of discussion in theoretical studies.[53,54] Although we do not know which surface structure is the most active for the La-based perovskite oxide system, we have provided XPS evidence that a higher O_{sur}/O_{latt} ratio correlates with higher electrocatalytic activity. With the progressive leaching of B-site cations during testing conditions, the remaining amorphous La oxide layer lowers the overall catalytic activity. Therefore, we propose a modified mechanism as an alternative to the more widely accepted alkaline ORR/OER catalytic cycle for La-based perovskite oxide catalysts (Figure 7).[17,25] Of course, in a highly alkaline environment, the leached B-site cations would more than likely be present in solution as hydroxide salts. With the B-site as the active yet unstable site, this mechanism acknowledges the irreversible leaching of B-site cations under standard testing conditions, which results in an irreversible decay in electrocatalytic activity. Thus, future efforts on these materials as alkaline ORR electrocatalysts should be directed toward stabilizing their interfaces, to potentially make them practical candidates for fuel cell and electrolyzer applications.

4. CONCLUSIONS

A family of La-based perovskite oxides including $LaCo_xM_{1-x}O_3$ (M = Mn, Ni; x = 1, 0.9, 0.5, 0.1, 0) has been synthesized, characterized, and tested for alkaline ORR activity. Some of them exhibited initial promising electrocatalytic activity, with $LaCoO_3$ exhibiting Levich and Koutecký−Levich values of $n \approx 4.0$ and j_k @ +0.8 V *vs* RHE ≈ 3.8 mA/cm^2, respectively. However, all of the compositions were degraded by ~0.30 mA/cm^2 and ~20 mV over just a few consecutive triangular potential cycles between +1.2 and +0.4 V *vs* RHE. Furthermore, pretesting and post-testing ORR ICP-AES, XPS, and STEM/EELS measurements on $LaCo_{0.9}Mn_{0.1}O_3$ confirmed the leaching of B-site cations and the formation of a 1−2 nm thick amorphous La oxide shell under standard testing conditions. Our findings were utilized to modify the conventionally accepted La-based perovskite oxide ORR mechanism, to include an irreversible side reaction (B-site cation leaching) that poses great challenges for these as-prepared materials as practical catalysts for the ORR in alkaline media. This work should also serve as a reminder of the importance of matching claims of promising catalytic activity with evidence of stability under testing conditions. Our current efforts focus on stabilizing these materials with the goal of promoting them to the realm of practical candidates for the alkaline fuel cell ORR and/or electrolyzer OER.

■ ASSOCIATED CONTENT

Supporting Information

The Supporting Information is available free of charge at https://pubs.acs.org/doi/10.1021/acs.jpcc.2c00108.

Synthesis; XRD; TEM; HAADF-STEM/EELS; ICP-AES; TGA; XPS; and additional figures (PDF)

■ AUTHOR INFORMATION

Corresponding Authors

Francis J. DiSalvo − *Department of Chemistry and Chemical Biology, Cornell University, Ithaca, New York 14853, United States*; Email: fjd3@cornell.edu

Héctor D. Abruña − *Department of Chemistry and Chemical Biology, Cornell University, Ithaca, New York 14853, United States*; orcid.org/0000-0002-3948-356X; Email: hda1@cornell.edu

Authors

Jeesoo Seok − *Department of Chemistry and Chemical Biology, Cornell University, Ithaca, New York 14853, United States*; orcid.org/0000-0002-9355-0751

Andrés Molina Villarino − *Department of Chemistry and Chemical Biology, Cornell University, Ithaca, New York 14853, United States*; orcid.org/0000-0003-3272-5156

Zixiao Shi − *Department of Chemistry and Chemical Biology, Cornell University, Ithaca, New York 14853, United States*

Yao Yang − *Department of Chemistry and Chemical Biology, Cornell University, Ithaca, New York 14853, United States*; orcid.org/0000-0003-0321-3792

Mahdi Ahmadi − *Department of Chemistry and Chemical Biology, Cornell University, Ithaca, New York 14853, United States*

David A. Muller − *School of Applied and Engineering Physics, Cornell University, Ithaca, New York 14853, United States*

Complete contact information is available at: https://pubs.acs.org/10.1021/acs.jpcc.2c00108

Author Contributions

[§] J.S. and A.M.V. contributed equally.

Notes

The authors declare no competing financial interest.

■ ACKNOWLEDGMENTS

The authors would like to greatly acknowledge the funding sources and facility centers that made this work possible: the National Science Foundation (NSF, DGE-1650441), the Center for Alkaline-Based Energy Solutions (CABES, DE-SC0019445), the Cornell Center for Materials Research (CCMR, DMR-1719875), and the Cornell Nutrient Analysis Laboratory (CNAL). Special thanks go to Muhammad (Mo) Salim for XPS data acquisition, Tatyana Dokuchayeva for ICP-AES data acquisition, Anthony Condo for TGA data acquisition, Michael Cao and Yu-Tsun Shao for part of the STEM/EELS data acquisition, and George E. Maio for helpful discussions on the project.

■ REFERENCES

(1) Working Group III Contribution to the Fifth Assessment Report of the Intergovernmental Panel on Climate Change. *Climate Change 2014: Mitigation of Climate Change*; Cambridge University Press: New York, NY, 2014.

(2) Hawkins, T. R.; Gausen, O. M.; Strømman, A. H. Environmental Impacts of Hybrid and Electric Vehicles—a Review. *Int. J. Life Cycle Assess.* **2012**, *17*, 997−1014.

(3) Perry, M. L.; Fuller, T. F. A Historical Perspective of Fuel Cell Technology in the 20th Century. *J. Electrochem. Soc.* **2002**, *149*, S59.

(4) Carrette, L.; Friedrich, K. A.; Stimming, U. Fuel Cells − Fundamentals and Applications. *Fuel Cells* **2001**, *1*, 5−39.

(5) Mekhilef, S.; Saidur, R.; Safari, A. Comparative Study of Different Fuel Cell Technologies. *Renewable Sustainable Energy Rev.* **2012**, *16*, 981−989.

(6) Lutz, A. E.; Larson, R. S.; Keller, J. O. Thermodynamic Comparison of Fuel Cells to the Carnot Cycle. *Int. J. Hydrogen Energy* **2002**, *27*, 1103−1111.

(7) Wee, J.-H. Applications of Proton Exchange Membrane Fuel Cell Systems. *Renewable Sustainable Energy Rev.* **2007**, *11*, 1720−1738.

(8) Dekel, D. R. Review of Cell Performance in Anion Exchange Membrane Fuel Cells. *J. Power Sources* **2018**, *375*, 158−169.

(9) Wei, C.; Rao, R. R.; Peng, J.; Huang, B.; Stephens, I. E. L.; Risch, M.; Xu, Z. J.; Shao-Horn, Y. Recommended Practices and Benchmark Activity for Hydrogen and Oxygen Electrocatalysis in Water Splitting and Fuel Cells. *Adv. Mater.* **2019**, *31*, No. 1806296.

(10) Arges, C. G.; Ramani, V. K.; Pintauro, P. N. The Chalkboard: Anion Exchange Membrane Fuel Cells. *Electrochem. Soc. Interface* **2010**, *19*, 31−35.

(11) Mohammadzadeh, K.; Khaleghi, H.; Abolfazli, H.; Seddiq, M. Effects of Gas Cross-over through the Membrane on Water Management in the Cathode and Anode Sides of PEM Fuel Cell. *J. Appl. Fluid. Mech.* **2018**, *11*, 861−875.

(12) Truc, N. T.; Ito, S.; Fushinobu, K. Numerical and Experimental Investigation on the Reactant Gas Crossover in a PEM Fuel Cell. *Int. J. Heat Mass Transfer* **2018**, *127*, 447−456.

(13) Ashok, A.; Kumar, A.; Bhosale, R. R.; Almomani, F.; Malik, S. S.; Suslov, S.; Tarlochan, F. Combustion Synthesis of Bifunctional $LaMO_3$ (M=Cr, Mn, Fe, Co, Ni) Perovskites for Oxygen Reduction and Oxygen Evolution Reaction in Alkaline Media. *J. Electroanal. Chem.* **2018**, *809*, 22−30.

(14) Royer, S.; Duprez, D. Catalytic Oxidation of Carbon Monoxide over Transition Metal Oxides. *ChemCatChem* **2011**, *3*, 24−65.

(15) Peña, M. A.; Fierro, J. L. G. Chemical Structures and Performance of Perovskite Oxides. *Chem. Rev.* **2001**, *101*, 1981−2018.

(16) Suntivich, J.; May, K. J.; Gasteiger, H. A.; Goodenough, J. B.; Shao-Horn, Y. A Perovskite Oxide Optimized for Oxygen Evolution Catalysis from Molecular Orbital Principles. *Science* **2011**, *334*, 1383−1385.

(17) Suntivich, J.; Gasteiger, H. A.; Yabuuchi, N.; Nakanishi, H.; Goodenough, J. B.; Shao-Horn, Y. Design Principles for Oxygen-Reduction Activity on Perovskite Oxide Catalysts for Fuel Cells and Metal−Air Batteries. *Nat. Chem.* **2011**, *3*, 546−550.

(18) Sakai, N.; Kawada, T.; Yokokawa, H.; Dokiya, M.; Iwata, T. Sinterability and Electrical Conductivity of Calcium-Doped Lanthanum Chromites. *J. Mater. Sci.* **1990**, *25*, 4531−4534.

(19) Zhu, H.; Zhang, P.; Dai, S. Recent Advances of Lanthanum-Based Perovskite Oxides for Catalysis. *ACS Catal.* **2015**, *5*, 6370−6385.

(20) Mustain, W. E.; Chatenet, M.; Page, M.; Seung Kim, Y. Durability Challenges of Anion Exchange Membrane Fuel Cells. *Energy Environ. Sci.* **2020**, *13*, 2805−2838.

(21) Schonvogel, D.; Hülstede, J.; Wagner, P.; Kruusenberg, I.; Tammeveski, K.; Dyck, A.; Agert, C.; Wark, M. Stability of Pt Nanoparticles on Alternative Carbon Supports for Oxygen Reduction Reaction. *J. Electrochem. Soc.* **2017**, *164*, No. F995.

(22) Lin, R.; Cai, X.; Zeng, H.; Yu, Z. Stability of High-Performance Pt-Based Catalysts for Oxygen Reduction Reactions. *Adv. Mater.* **2018**, *30*, No. 1705332.

(23) Banham, D.; Ye, S.; Pei, K.; Ozaki, J.; Kishimoto, T.; Imashiro, Y. A Review of the Stability and Durability of Non-Precious Metal Catalysts for the Oxygen Reduction Reaction in Proton Exchange Membrane Fuel Cells. *J. Power Sources* **2015**, *285*, 334−348.

(24) Risch, M. Perovskite Electrocatalysts for the Oxygen Reduction Reaction in Alkaline Media. *Catalysts* **2017**, *7*, No. 154.

(25) Hong, W. T.; Risch, M.; A. Stoerzinger, K.; Grimaud, A.; Suntivich, J.; Shao-Horn, Y. Toward the Rational Design of Non-Precious Transition Metal Oxides for Oxygen Electrocatalysis. *Energy Environ. Sci.* **2015**, *8*, 1404−1427.

(26) Komo, M.; Hagiwara, A.; Taminato, S.; Hirayama, M.; Kanno, R. Oxygen Evolution and Reduction Reactions on $La_{0.8}Sr_{0.2}CoO_3$ (001), (110), and (111) Surfaces in an Alkaline Solution. *Electrochemistry* **2012**, *80*, 834−838.

(27) Cueva, P.; Hovden, R.; Mundy, J. A.; Xin, H. L.; Muller, D. A. Data Processing for Atomic Resolution Electron Energy Loss Spectroscopy. *Microsc. Microanal.* **2012**, *18*, 667−675.

(28) Baythoun, M. S. G.; Sale, F. R. Production of Strontium-Substituted Lanthanum Manganite Perovskite Powder by the Amorphous Citrate Process. *J. Mater. Sci.* **1982**, *17*, 2757−2769.

(29) Fita, I.; Markovich, V.; Mogilyansky, D.; Puzniak, R.; Wisniewski, A.; Titelman, L.; Vradman, L.; Herskowitz, M.; Varyukhin, V. N.; Gorodetsky, G. Size-and Pressure-Controlled Ferromagnetism in $LaCoO_3$ Nanoparticles. *Phys. Rev. B* **2008**, *77*, No. 224421.

(30) Danks, A. E.; Hall, S. R.; Schnepp, Z. J. M. H. The Evolution of 'Sol−Gel' Chemistry as a Technique for Materials Synthesis. *Mater. Horiz.* **2016**, *3*, 91−112.

(31) Bernard, C.; Laberty, C.; Ansart, F.; Durand, B. Hydrothermal Synthesis of $La_{1-X}Sr_xMnO_{3+\delta}$ Manganites. *Ann. Chim. Sci. Mater.* **2003**, *28*, 85−96.

(32) Chan, K. S.; Ma, J.; Jaenicke, S.; Chuah, G. K.; Lee, J. Y. Catalytic Carbon Monoxide Oxidation over Strontium, Cerium and Copper-Substituted Lanthanum Manganates and Cobaltates. *Appl. Catal., A* **1994**, *107*, 201−227.

(33) Zhou, W.; Sunarso, J. Enhancing Bi-Functional Electrocatalytic Activity of Perovskite by Temperature Shock: A Case Study of $LaNiO_{3-\delta}$. *J. Phys. Chem. Lett.* **2013**, *4*, 2982−2988.

(34) Goldschmidt, V. M. Die Gesetze der Krystallochemie. *Naturwissenschaften* **1926**, *14*, 477−485.

(35) Travis, W.; Glover, E. N. K.; Bronstein, H.; Scanlon, D. O.; Palgrave, R. G. On the Application of the Tolerance Factor to Inorganic and Hybrid Halide Perovskites: A Revised System. *Chem. Sci.* **2016**, *7*, 4548−4556.

(36) Shannon, R. D. Revised Effective Ionic Radii and Systematic Studies of Interatomic Distances in Halides and Chalcogenides. *Acta Crystallogr., Sect. A* **1976**, *32*, 751−767.

(37) Kuno, M. Hybrid Preparations. In *Introductory Nanoscience: Physical and Chemical Concepts*; Garland Science: New York, 2012; p 353.

(38) Liu, X.; Gong, H.; Wang, T.; Guo, H.; Song, L.; Xia, W.; Gao, B.; Jiang, Z.; Feng, L.; He, J. Cobalt-Doped Perovskite-Type Oxide

$LaMnO_3$ as Bifunctional Oxygen Catalysts for Hybrid Lithium−Oxygen Batteries. *Chem. - Asian J.* **2018**, *13*, 528−535.

(39) Chen, D.; Chen, C.; Baiyee, Z. M.; Shao, Z.; Ciucci, F. Nonstoichiometric Oxides as Low-Cost and Highly-Efficient Oxygen Reduction/Evolution Catalysts for Low-Temperature Electrochemical Devices. *Chem. Rev.* **2015**, *115*, 9869−9921.

(40) Rizo, R.; Herrero, E.; Feliu, J. M. Oxygen Reduction Reaction on Stepped Platinum Surfaces in Alkaline Media. *Phys. Chem. Chem. Phys.* **2013**, *15*, 15416−15425.

(41) Lopes, P. P.; Chung, D. Y.; Rui, X.; Zheng, H.; He, H.; Farinazzo Bergamo Dias Martins, P.; Strmcnik, D.; Stamenkovic, V. R.; Zapol, P.; Mitchell, J. F.; et al. Dynamically Stable Active Sites from Surface Evolution of Perovskite Materials during the Oxygen Evolution Reaction. *J. Am. Chem. Soc.* **2021**, *143*, 2741−2750.

(42) Speight, J. *Lange's Handbook of Chemistry*, 16th ed.; McGraw-Hill Education: New York, 2005.

(43) Hasché, F.; Oezaslan, M.; Strasser, P. Activity, Stability, and Degradation Mechanisms of Dealloyed $PtCu_3$ and $PtCo_3$ Nanoparticle Fuel Cell Catalysts. *ChemCatChem* **2011**, *3*, 1805−1813.

(44) Yin, J.-W.; Yin, Y.-M.; Lu, J.; Zhang, C.; Minh, N. Q.; Ma, Z.-F. Structure and Properties of Novel Cobalt-Free Oxides $Nd_xSr_{1-X}Fe_{0.8}Cu_{0.2}O_{3-\delta}$ ($0.3 \le x \le 0.7$) as Cathodes of Intermediate Temperature Solid Oxide Fuel Cells. *J. Phys. Chem. C* **2014**, *118*, 13357−13368.

(45) Arandiyan, H.; Dai, H.; Deng, J.; Liu, Y.; Bai, B.; Wang, Y.; Li, X.; Xie, S.; Li, J. Three-Dimensionally Ordered Macroporous $La_{0.6}Sr_{0.4}MnO_3$ with High Surface Areas: Active Catalysts for the Combustion of Methane. *J. Catal.* **2013**, *307*, 327−339.

(46) Yamazoe, N.; Teraoka, Y.; Seiyama, T. TPD and XPS Study on Thermal Behavior of Absorbed Oxygen in $La_{1-x}Sr_xCoO_3$. *Chem. Lett.* **1981**, *10*, 1767−1770.

(47) Stoerzinger, K. A.; Hong, W. T.; Crumlin, E. J.; Bluhm, H.; Biegalski, M. D.; Shao-Horn, Y. Water Reactivity on the $LaCoO_3$ (001) Surface: An Ambient Pressure X-Ray Photoelectron Spectroscopy Study. *J. Phys. Chem. C* **2014**, *118*, 19733−19741.

(48) Merino, N. A.; Barbero, B. P.; Eloy, P.; Cadús, L. E. $La_{1-x}Ca_xCoO_3$ Perovskite-Type Oxides: Identification of the Surface Oxygen Species by XPS. *Appl. Surf. Sci.* **2006**, *253*, 1489−1493.

(49) Imamura, M.; Matsubayashi, N.; Shimada, H. Catalytically Active Oxygen Species in $La_{1-x}Sr_xCoO_{3-\delta}$ Studied by XPS and XAFS Spectroscopy. *J. Phys. Chem. B* **2000**, *104*, 7348−7353.

(50) Schulze, M.; Lorenz, M.; Wagner, N.; Gülzow, E. XPS Analysis of the Degradation of Nafion. *Fresenius' J. Anal. Chem.* **1999**, *365*, 106−113.

(51) Muller, D. A.; Sorsch, T.; Moccio, S.; Baumann, F. H.; Evans-Lutterodt, K.; Timp, G. The Electronic Structure at the Atomic Scale of Ultrathin Gate Oxides. *Nature* **1999**, *399*, 758−761.

(52) Bak, J.; Bae, H. B.; Chung, S.-Y. Atomic-Scale Perturbation of Oxygen Octahedra via Surface Ion Exchange in Perovskite Nickelates Boosts Water Oxidation. *Nat. Commun.* **2019**, *10*, No. 2713.

(53) Lee, Y.-L.; Gadre, M. J.; Shao-Horn, Y.; Morgan, D. Ab Initio GGA+*U* Study of Oxygen Evolution and Oxygen Reduction Electrocatalysis on the (001) Surfaces of Lanthanum Transition Metal Perovskites $LaBO_3$ (B = Cr, Mn, Fe, Co and Ni). *Phys. Chem. Chem. Phys.* **2015**, *17*, 21643−21663.

(54) Mastrikov, Y. A.; Merkle, R.; Kotomin, E. A.; Kuklja, M. M.; Maier, J. Surface Termination Effects on the Oxygen Reduction Reaction Rate at Fuel Cell Cathodes. *J. Mater. Chem. A* **2018**, *6*, 11929−11940.

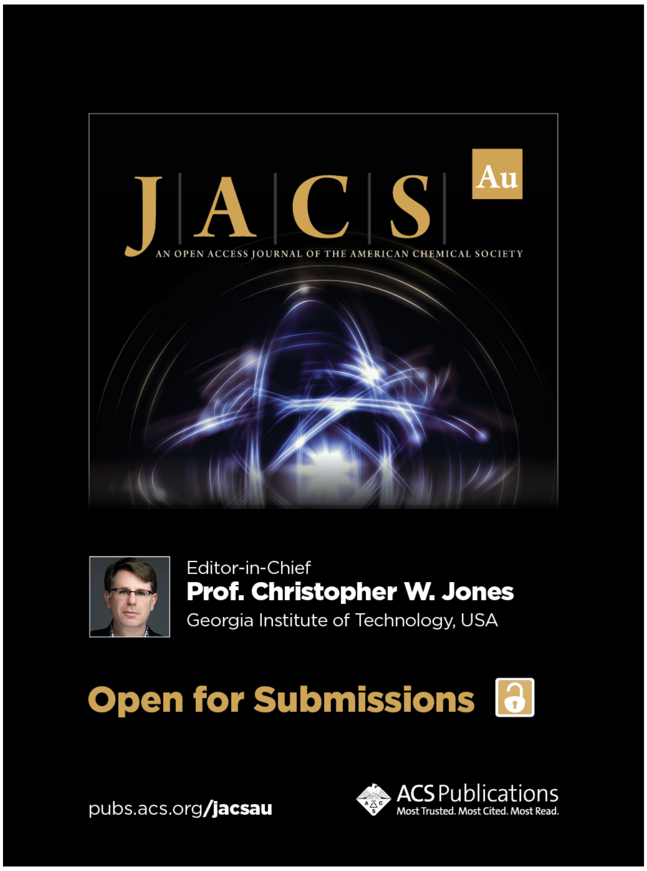

https://doi.org/10.1021/acs.jpcc.2c00108
J. Phys. Chem. C XXXX, XXX, XXX−XXX